

Supplementary information

Spin-spin interactions and spin delocalisation in a doped organic semiconductor probed by EPR spectroscopy

Claudia E. Tait,^{*a,b} Anna Reckwitz,^a Malavika Arvind,^c Dieter Neher,^c Robert Bittl,^a and Jan Behrends^{*a}

^a Department of Physics, Freie Universität Berlin, Arnimallee 14, 14195 Berlin, Germany.

^b Physical and Theoretical Chemistry Laboratory, Department of Chemistry, University of Oxford, South Parks Road, OX1 3QZ Oxford, United Kingdom.

^c Institute of Physics and Astronomy, Universität Potsdam, Karl-Liebknecht-Str. 24-25, 14476 Potsdam, Germany.

S1 Materials and experimental methods

S1.1 Materials and sample preparation

Poly(3-hexylthiophene-2,5-diyl) (P3HT, >96% regioregularity, weight-average molecular weight M_w of ca. 40 kDa, polydispersity index (PDI) of 2.1, Rieke Metals, RMI-001EE) was used for doping studies with tris(pentafluorophenyl)borane (BCF, 98% purity, Tokyo Chemical Industry) and 2,3,5,6-tetrafluoro-7,7,8,8-tetracyanoquinodimethane (F_4 TCNQ, 97% purity, Sigma-Aldrich). Solutions were prepared in chloroform (CF, anhydrous, $\geq 99\%$, Sigma-Aldrich) or in *o*-dichlorobenzene (oDCB, anhydrous, $\geq 99\%$, Sigma-Aldrich). The sample preparation was performed in an inert N_2 atmosphere.

Solutions and films of doped P3HT prepared from chloroform were obtained by mixing stock solutions of 6 mg mL^{-1} P3HT (stirred at 40°C until dissolved) with 2 mg mL^{-1} BCF or 0.5 mg mL^{-1} F_4 TCNQ in different proportions to achieve doping ratios of 10^3 , $2.5 \cdot 10^3$, $5 \cdot 10^3$, 10^2 , $2.5 \cdot 10^2$, $5 \cdot 10^2$ and 10^1 . Solutions and films of doped P3HT prepared from *o*-dichlorobenzene were obtained by mixing stock solutions of 4 mg mL^{-1} P3HT (stirred at 40°C until dissolved) with 2 mg mL^{-1} BCF or 1 mg mL^{-1} F_4 TCNQ in different proportions to achieve the desired doping ratios. For both solvents, all final solutions were at a constant concentration of P3HT of 2 mg mL^{-1} (ca. 11.9 mM).

Samples for the X- and Q-band EPR measurements were prepared by transferring $25 \mu\text{L}$ of doped P3HT solution into 2.9 mm OD, 2.2 mm ID quartz tubes shortly after mixing. The solvent was evaporated under vacuum to create a film on the inside of the EPR tube, followed by back-filling with helium and flame-sealing of the tube. The film samples were stored at -80°C between measurements.

For solution measurements, the tubes were sealed with critoseal[®] and stored inside the glove box until the EPR measurements (performed within a couple of hours from mixing of the solutions, except for the measurements on P3HT solutions doped with BCF in chloroform, which were performed on the next day due to slower doping for BCF in this solvent¹).

Samples for the W-band measurements were prepared by trans-

ferring $1\text{-}2 \mu\text{L}$ of doped P3HT solution into 0.87 mm OD, 0.7 mm ID quartz tubes, evaporating the solvent under vacuum and sealing the tube with critoseal[®] inside a glove box. Powder samples were prepared from drop-cast films by scratching fragments of the films off a glass substrate and transferring them into 0.87 mm OD, 0.7 mm ID quartz tubes that were subsequently sealed with critoseal[®]. The quality of the powder samples was verified by checking for invariance of the recorded EPR spectrum for two different sample orientations differing by 90° .

For reference measurements on the radical anion of F_4 TCNQ, F_4 TCNQ was dissolved in deuterated tetrahydrofuran ($\text{THF-}d_8$) (0.5 to 2 mM) resulting in partial reduction to the radical anion, as verified by UV-vis measurements.¹ Measurements were performed on solutions and on films generated by solvent evaporation.

S1.2 Continuous wave EPR measurements

X-band continuous wave EPR measurements were performed on a laboratory-built spectrometer consisting of a Bruker ER 041 MR microwave bridge with an ER 048 R microwave controller and an AEG electromagnet with a Bruker BH15 Hall effect field controller, using a Bruker ER 4122 SHQE resonator. A Stanford Research SR810 lock-in amplifier in combination with a Wangine WPA-120 modulation amplifier was used for field modulation and lock-in detection. Low temperature measurements were performed with a continuous flow helium cryostat (ESR900, Oxford Instruments) and temperature controller (ITC503, Oxford Instruments). The field was calibrated with a standard $N@C_{60}$ sample with a known *g*-value.² Spin quantification was performed with reference to a standard sample of TEMPOL in toluene with a known spin concentration, taking into account the quality factor (*Q*-factor) of the resonator, determined from a Lorentzian fit of the mode picture recorded for each measurement.³ Spin concentrations were calculated based on the mass of P3HT in a sample and assuming a mass density $\rho = 1.1 \text{ g cm}^{-3}$ for P3HT⁴ (resulting in a number density of $4 \cdot 10^{27}$ thiophene units per m^3). The spectra were acquired at a microwave frequency of ca. 9.4 GHz at a microwave power adjusted to well below satu-

ration for the different samples and measurement temperatures. A 100 kHz modulation frequency and modulation amplitudes of 0.040 mT and 0.025 mT/0.150 mT were used for the film samples of P3HT:BCF and P3HT:F₄TCNQ (CF/oDCB), respectively. W-band continuous wave EPR measurements were performed on a Bruker ElexSys E680 spectrometer with a Teraflex EN600-1021H resonator and equipped with a helium-flow cryostat. The spectra were acquired at a microwave frequency of ca. 94 GHz with a microwave power of 9.98 μ W, a modulation frequency of 100 kHz and modulation amplitudes of 0.10 to 0.20 mT. A background correction was performed using a reference measurement on the empty resonator. Field calibration was again performed with a N@C₆₀ standard sample.²

S1.3 Pulse EPR measurements

Pulse EPR measurements were performed at Q-band on a Bruker ElexSys E580 spectrometer with a home-built Q-band ENDOR resonator with large sample access (3 mm).⁵ The measurements were performed at cryogenic temperatures (10 K unless otherwise specified) using a continuous-flow helium cryostat and temperature-control system from Oxford Instruments.

Pulse EPR spectra were recorded as echo-detected field sweeps using a Hahn echo sequence with pulse lengths of $t_{\pi/2} = 32$ ns and $t_{\pi} = 64$ ns, an inter-pulse delay τ of 400 ns, a two-step phase cycle and an echo integration window of 330 ns. Additionally, echo transients were also recorded separately, Fourier transformed and projected onto the magnetic field axis to obtain the EPR spectrum following the procedure described by Bowman et al.⁶ to avoid distortions observed in the spectra obtained by echo integration for BCF-doped P3HT at high doping concentrations. For highly doped film samples, a strong FID signal was observed and FID-detected EPR spectra were measured by recording the FID after a 32 ns or 200 ns $\frac{\pi}{2}$ pulse with a four-step phase cycle, followed again by Fourier transformation and projection onto the field axis.⁶

Echo decay measurements were performed using the pulse sequence $\frac{\pi}{2} - \tau - \pi - \tau$ -echo with $t_{\pi/2} = 32$ ns, $t_{\pi} = 64$ ns, $\tau_0 = 200$ ns and a two-step phase cycle.

Inversion recovery measurements were performed with an initial inversion pulse of $t_{\pi,inv} = 64$ ns and an echo detection sequence with $t_{\pi/2} = 64$ ns, $t_{\pi} = 128$ ns and $\tau = 400$ ns. FID-detected inversion recovery measurements were performed using a $t_{\pi/2} = 200$ ns or $t_{\pi/2} = 32$ ns detection pulse. Typically, two or more inversion recovery traces with different time increments and lengths were recorded and stitched together.

Davies ENDOR measurements were performed with the pulse sequence $\pi - T - \frac{\pi}{2} - \tau - \pi - \tau$ -echo with $t_{\pi/2} = 64$ ns, $t_{\pi} = 128$ ns, $\tau = 300$ ns and a 23 μ s radiofrequency π pulse applied during the delay T . The radiofrequency pulse length was adjusted for ¹H using a Rabi nutation experiment.

Three-pulse ESEEM measurements were performed with the pulse sequence $\frac{\pi}{2} - \tau - \frac{\pi}{2} - T - \frac{\pi}{2} - \tau$ -echo with $t_{\pi/2} = 32$ ns and $\tau = 140, 180$ and 240 ns. The delay T was incremented from 64 ns with steps of 8 ns and an eight-step phase cycle was used to remove unwanted contributions from crossing echoes. The time-

domain ESEEM data was baseline corrected using a stretched exponential and the frequency-domain spectra were obtained after apodisation with a Hamming window, zero-filling and Fourier transform using the cross-term averaging procedure⁷ as implemented in EasySpin.⁸

Nutation experiments were performed using the PEANUT pulse sequence⁹ $\frac{\pi}{2} - \tau - \text{HTA}(+x) - \text{HTA}(-x) - \tau$ -echo with $t_{\pi/2} = 60$ ns, $\tau = 300$ ns and an overall length of the HTA pulse of 3 μ s. The microwave power during the HTA pulse was adjusted to correspond to a π pulse length of approximately 24 ns for an $S = \frac{1}{2}$ signal. The position of the phase inversion was incremented from $t_0 = 1 \mu$ s to 2 μ s with increments $\Delta t = 2$ ns. A two-step phase cycle on the first pulse was used to remove unwanted contributions. The frequency-domain nutation spectra were obtained from the acquired time-domain data after polynomial baseline correction, apodisation with a Hamming window, zero-filling and Fourier transformation.

S1.4 Data analysis and spectral simulations

Spectral simulations of the cw EPR, ENDOR and three-pulse ESEEM data were performed with the EasySpin^{8,10} Matlab toolbox.

S1.4.1 Simulations of cw EPR spectra with partial alignment

Simulations of the cw EPR spectra for the BCF-doped P3HT films deposited on the inside of EPR tubes under consideration of partial alignment of the P3HT molecules were performed by approximating the cylindrical geometry of the inner wall film spectrum as the sum over spectra of a planar substrate rotated with respect to the sample tube axis ($z_{\text{sample}} \perp B$, see Fig. 3 in the main text). Two possible orientations of the g -matrix frame, as well as the molecular frame, with respect to the substrate expected for edge-on orientations of P3HT are depicted in Fig. 3 of the main text. For the simulations the orientation of the principal g -axes with respect to the substrate frame was defined by three angles.

The EPR spectra were obtained by generating a complete set of orientations of the P3HT g -matrix in the substrate frame and computing the corresponding spectra using EasySpin, considering rotation of the substrate around the sample axis from 0° (magnetic field B in the substrate plane) to 90° (magnetic field B perpendicular to the substrate plane) in 5° increments. The spectra were then weighted by an orientational distribution function $F(\Omega)$, where Ω corresponds to the three angles defining the orientation of the g -matrix in the substrate frame, determined by a Gaussian probability distribution for each angle. A least-squares fitting routine was used to determine the centre and FWHM for each angular distribution giving the best agreement with the experimental results. A convolutional broadening was used as additional fitting parameter, while the principal g -values were fixed at the values determined from the low temperature W-band powder EPR spectra ($g_x = 2.0029$, $g_y = 2.0020$ and $g_z = 2.0010$).

The probability distribution of the g_z axis orientation (parallel to the polymer backbone) in the laboratory frame is shown in the insets of Fig. 3 in the main text for the best fit orientational distribution function.

S1.4.2 Determination of spin delocalisation from ENDOR.

The ^1H ENDOR data was simulated following the approach used by Aguirre et al.¹¹ for the analysis of ENDOR spectra of I_2 -doped P3HT films, and previously used to determine the extent of spin delocalisation in doped regioregular and regiorandom P3HT in solution.¹ Since the hyperfine coupling of aromatic α -protons is determined by spin polarization in the C-H bond, the isotropic hyperfine coupling a_{iso} can be directly estimated from the spin density on the adjacent carbon atom, ρ_C , using the McConnell equation

$$a_{\text{iso}} = Q\rho_C \quad (\text{S1})$$

where Q is the McConnell constant.¹² The full anisotropic hyperfine coupling for α -protons in π -electron systems can be modelled using the following equations:¹³

$$A_x = (1 - \alpha) a_{\text{iso}} \quad A_y = (1 + \alpha) a_{\text{iso}} \quad A_z = a_{\text{iso}} \quad (\text{S2})$$

where α is an anisotropy parameter, usually assumed to be ca. 0.5, and the principal hyperfine axes are determined by the out-of-plane axis of the aromatic system (z), the in-plane axis parallel to the C-H bond (x) and the in-plane axis perpendicular to the C-H bond (y) (see Fig. 1 in the main text).

In order to determine the spin density distribution from the ENDOR data and take the uncertainties of the parameters used for estimating the hyperfine couplings into account, a library of ENDOR spectra was generated and compared to the experimental spectra. The library contained spectra calculated for a range of different distributions of the spin density on the P3HT backbone using values of Q , $\rho_C/\rho_{\text{thiophene}}$ and α randomly varied within their estimated uncertainty intervals. The distributions within a factor two of the root-mean square deviation between the experimental data and the best-fit simulation were then considered to describe the extent of delocalisation on the P3HT backbone.

Based on data from quantum chemical calculations,^{14,15} spin density distributions with different extents of delocalisation over a number N of thiophene rings were modelled with Gaussian or super-Gaussian functions

$$y = \exp\left(-\left(\frac{-4 \ln 2 (x - x_0)^2}{\text{FWHM}^2}\right)^n\right) \quad (\text{S3})$$

where FWHM is the full-width at half maximum (for $n = 1$) and the order n was varied between 1 (Gaussian) and 3 (distribution with a flat top). The hyperfine couplings of the α -protons on the P3HT backbone were then calculated based on equations (S1) and (S2) assuming $\rho_C = 0.23 \pm 0.02 \rho_{\text{thiophene}}$, $Q = -72.9 \pm 0.5$ MHz and $\alpha = 0.50 \pm 0.05$ (based on reference 11).

The ENDOR spectra were simulated with EasySpin using the estimated hyperfine values and the relative orientations of the principal g - and A -axes depicted in Fig. 1 (Euler angles for transformation from the g - to the A -frame: $\alpha = 90^\circ$, $\beta = 90^\circ$ and $\gamma = -57^\circ$). The principal g -values for P3HT used in the simulations were $g_x = 2.0029$, $g_y = 2.0020$ and $g_z = 2.0010$ and the ENDOR spectra were simulated for a field position corresponding to the maximum of the EPR spectrum. The resulting simulations were multiplied by the Davies ENDOR blind-spot function

to account for the suppression of small hyperfine couplings.¹⁶ For a better fit of the ENDOR spectra of the doped P3HT films, the library of model distributions also contained weighted sums of distributions with different FWHM values.

S1.4.3 PEANUT simulations.

The PEANUT data for a coupled spin pair was simulated using a home-written Matlab program that solves the Liouville-von Neumann equation and is based on the EasySpin pulse EPR simulation routines.^{10,17} The static Hamiltonian used in the simulations included the electron Zeeman interactions for the two spin centres, a dipolar electron-electron interaction and the exchange coupling between the two spins:

$$\mathcal{H} = \frac{\mu_B}{h} \mathbf{B} g_1 \mathbf{S}_1 + \frac{\mu_B}{h} \mathbf{B} g_2 \mathbf{S}_2 + \mathbf{S}_1 \mathbf{D} \mathbf{S}_2 + J \mathbf{S}_1 \mathbf{S}_2 \quad (\text{S4})$$

The simulations were performed in a rotating frame offset by 0.6 GHz from the microwave frequency of the experiment and included powder averaging over all three Euler angles defining the relative orientation of the laboratory and molecular frames. The pulse sequence parameters used in the simulations matched the parameters used in the experiment. The principal g -values used were $g_x = 2.0029$, $g_y = 2.0020$ and $g_z = 2.0010$ for P3HT and $g_x = 2.0030$, $g_y = 2.0030$ and $g_z = 2.0024$ for F_4TCNQ (see Fig. 1 in the main text for the orientation of the g -matrix with respect to the molecular structure). The relative orientations of the g - and the dipolar interaction frames were chosen to model the relative orientations of the P3HT backbone and the F_4TCNQ molecule in doped films determined by Hamidi-Sakr et al.¹⁸

S2 Additional supporting data and figures

S2.1 Doping of P3HT with BCF

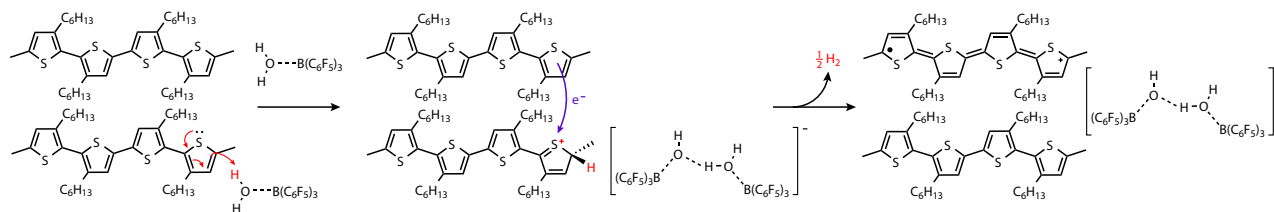


Fig. S1 Proposed reaction mechanism for doping of P3HT with BCF involving protonation of a polymer segment by a BCF(OH₂) complex followed by electron transfer from a different polymer segment resulting in formation of the P3HT radical cation observed by EPR and elimination of H₂ from the protonated chain segment, returning the neutral polymer.^{1,19} Marqués et al. concluded from a theoretical study that stabilisation of [BCF(OH)]⁻ by complexation with another BCF molecule, resulting in complexes of the type [BCF(OH)(OH₂)BCF]⁻ or [BCF(OH)BCF]⁻, is required for the protonation step to be feasible.¹⁹ They also propose various scenarios for H₂ elimination through reaction of two neutral protonated radicals, two protonated cationic polymers or a neutral and a cationic protonated polymer.¹⁹

S2.2 X-band continuous-wave EPR

Fig. S2 shows a comparison of the normalised room temperature X-band cw EPR spectra recorded for the BCF- and F_4TCNQ -doped P3HT films. The spectra obtained for the BCF-doped P3HT films can be simulated by taking the full g -matrix with the principal values of $g_x = 2.0029$, $g_y = 2.0020$ and $g_z = 2.0010$ determined from the W-band cw EPR spectra as well as partial alignment of the P3HT backbones into account. A reasonable agreement with the experimental spectra for F_4TCNQ -doped P3HT films prepared from oDCB can be obtained both for simulations taking separate contributions of the F_4TCNQ radical anion and the P3HT radical cation into account as well as for simulations performed for exchange-coupled spins on F_4TCNQ and P3HT with $|J| \gg |g_1 - g_2| \mu_B B$. In both cases a Lorentzian convolutional broadening was used in the simulations. While for low doping ratios simulations performed for a linear combination of spectra reproduce the experimentally observed asymmetries slightly better, the large linewidth and absence of any distinguishing features for higher doping ratios does not allow any conclusions regarding the spectral assignment based on the X-band cw EPR data. For F_4TCNQ -doped P3HT films prepared from CF, similar conclusions can be drawn for the lowest and highest doping ratios, however, the experimental spectra observed for intermediate doping ratios can only be simulated by considering exchange-coupled spins on F_4TCNQ and P3HT.

The room temperature cw EPR spectra recorded for solutions of doped P3HT and the corresponding films are compared in Fig. S3. In contrast to the EPR spectra recorded for F_4TCNQ -doped P3HT films, the EPR spectra for the corresponding solutions include a contribution of free F_4TCNQ radical anions with a resolved hyperfine structure attributed to the coupling to the four equivalent

nitrogen and the four equivalent fluorine nuclei in this molecule.¹ The relative contribution of free $F_4TCNQ^{\bullet-}$ amounts to about 1% for both F_4TCNQ -doped P3HT in oDCB and CF and decreases slightly with increasing doping ratios.

The variation of the resonator Q -values as a function of doping ratio for the different investigated film samples are compared in Fig. S4. Sample conductivity contributes to the loaded Q of an EPR resonator,³ and since all other contributions are equivalent for the investigated samples the changes in the Q -value determined from the reflected power as a function of microwave frequency can be attributed to changes in the conductivity of the P3HT films. The decrease in Q -values for increasing doping ratios observed for all samples indicates increased conductivity, in agreement with conductivity measurements reported on doped films in the literature. The temperature-dependence of the Q -values is also shown in Fig. S4 and reveals a decrease in conductivity for decreasing temperatures. Below about 50 K, no differences between doped films at different doping ratios and for different dopant-solvent combinations are observed.

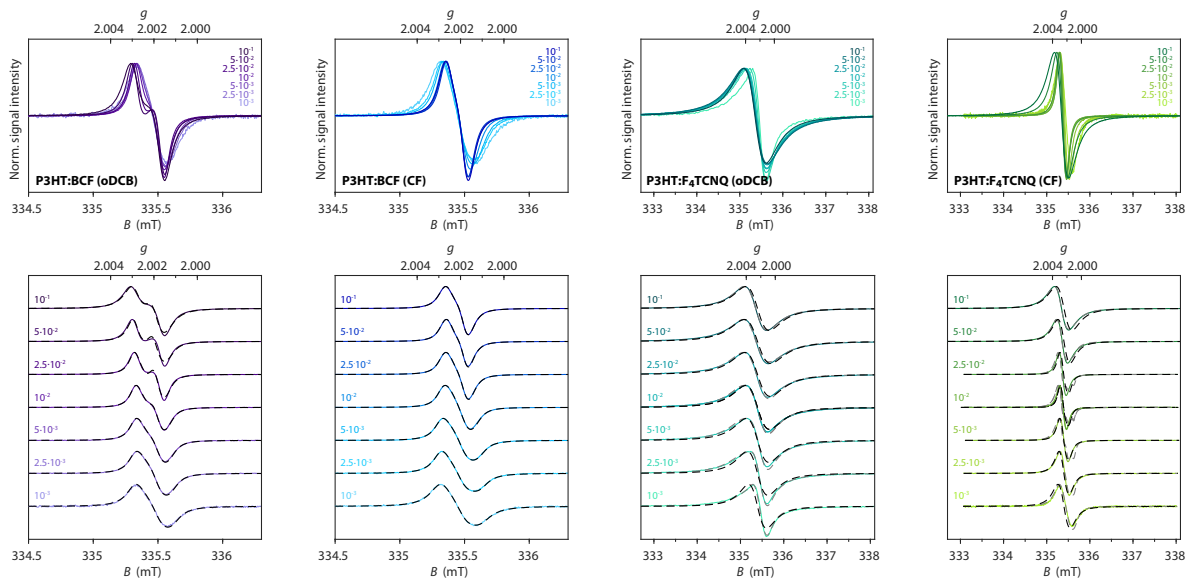


Fig. S2 (top) Comparison of the spectral shapes of the X-band room temperature cw EPR spectra recorded for BCF- and F_4TCNQ -doped P3HT films at different doping ratios (prepared from oDCB or CF). (bottom) Comparison of the experimental results (solid coloured lines) with simulations (dashed black lines) performed for the P3HT radical cation with $g_x = 2.0029$, $g_y = 2.0020$ and $g_z = 2.0010$ and with partial alignment of the P3HT chains for the BCF-doped samples and for a linear combination of P3HT and F_4TCNQ signals (dashed grey lines) and for exchange-coupled P3HT and F_4TCNQ radicals (dashed black lines) for the F_4TCNQ -doped samples.

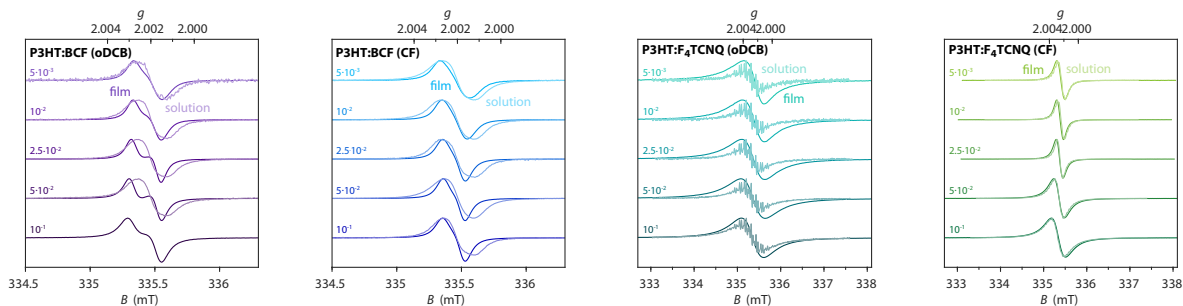


Fig. S3 Comparison of the spectral shapes of the X-band room temperature cw EPR spectra recorded for BCF- and F₄TCNQ-doped P3HT solutions in oDCB and CF and the corresponding films at different doping ratios.

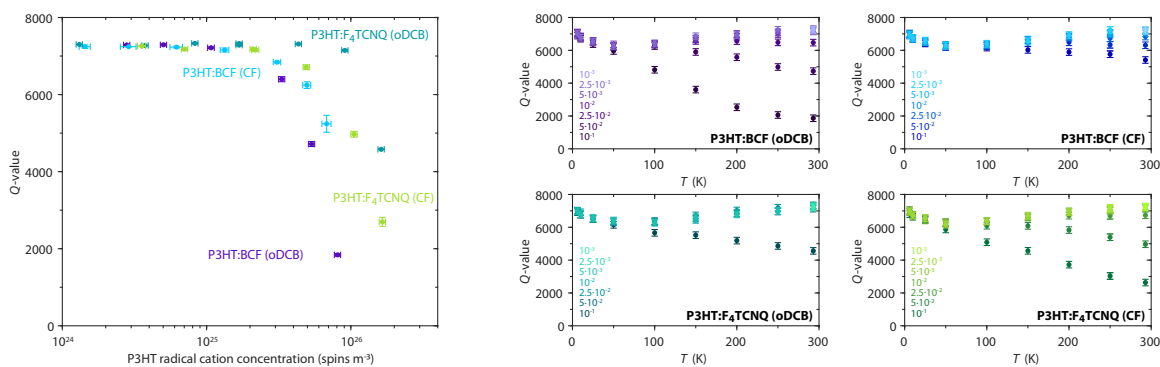


Fig. S4 Resonator Q -values measured at X-band for doped P3HT films deposited on the inside of a 2.9 mm OD, 2.2 mm ID quartz EPR tube. (left) Q -values as a function of the concentration of P3HT radical cations determined from the EPR spectra for BCF- and F₄TCNQ-doped P3HT films prepared from oDCB or CF. (right) Changes in Q -value with temperature in the range from 6 K to room temperature for each dopant-solvent combination. The Q -value of the empty resonator at room temperature typically corresponds to about 7500.

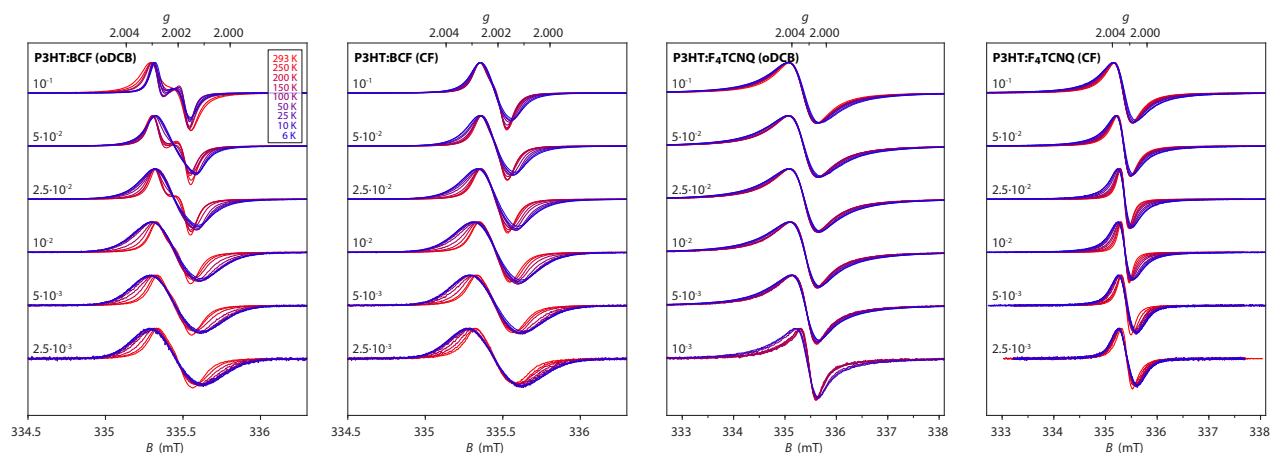


Fig. S5 Comparison of EPR spectra recorded at different temperatures within the range from 6 K to room temperature for BCF- and F₄TCNQ-doped P3HT films prepared from oDCB or CF (the displayed spectra are normalised to the maximum to highlight changes in spectral shape).

S2.3 Relaxation time measurements

The results of echo-decay and inversion recovery measurements performed on the BCF- and F₄TCNQ-doped P3HT films at different doping ratios at Q-band at $T = 10$ K are shown in Fig. S6. The relaxation traces were recorded at a field position corresponding to the maximum of the P3HT radical cation EPR signal, only small differences in spin-spin and spin-lattice relaxation times were evident from measurements at other field positions (see Fig. S7 for the results of field-dependent inversion recovery measurements on representative samples).

The phase memory times T_m were determined from a stretched exponential fit of the echo decay traces:

$$I(2\tau) = \exp\left(-\left(\frac{2\tau}{T_m}\right)^x\right) \quad (\text{S5})$$

The spin-lattice relaxation times T_1 were estimated from biexponential fits of inversion recovery traces, compared to the experimental data in Fig. S6. The experimental results could not be fitted adequately with a monoexponential function and no significant improvement was obtained by including more than two exponential terms. Given the heterogeneity of the spin environments expected for film samples and demonstrated by the EPR results of this study, the inversion recovery measurements likely contain contributions from spin centres with a range of different relaxation times and this distribution of relaxation times leads to the observed apparent biexponential behaviour. The two T_1 values determined from the biexponential fits and shown in Fig. 6 in the main text should therefore be considered to approximately

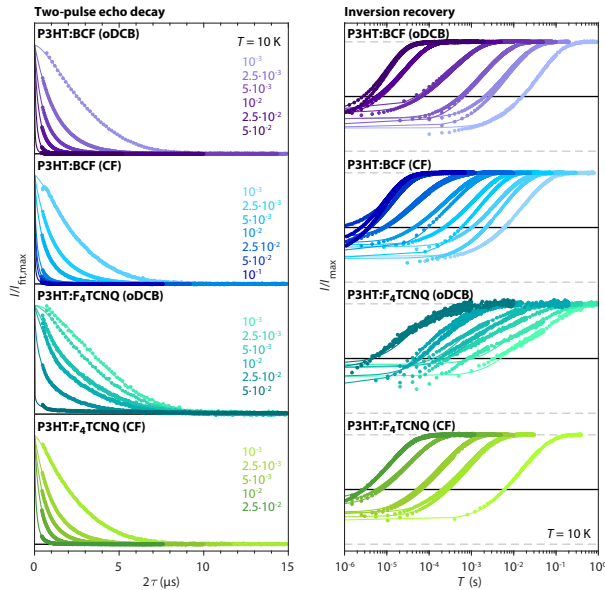


Fig. S6 Relaxation time measurements for BCF- and F₄TCNQ-doped P3HT films (prepared from oDCB or CF) at Q-band ($T = 10$ K). (*left*) Echo decay traces and stretched exponential fits. The decay traces were normalised to the intensity at $\tau = 0$ ns extrapolated from the fits. (*right*) Inversion recovery traces and biexponential fits. The traces are normalised with respect to the mean intensity after complete recovery. All measurements shown here were recorded at a field position corresponding to the maximum of the P3HT EPR spectrum (ca. 1213.4 mT).

define the range of relaxation times for film samples with a given doping concentration rather than actual T_1 relaxation times.

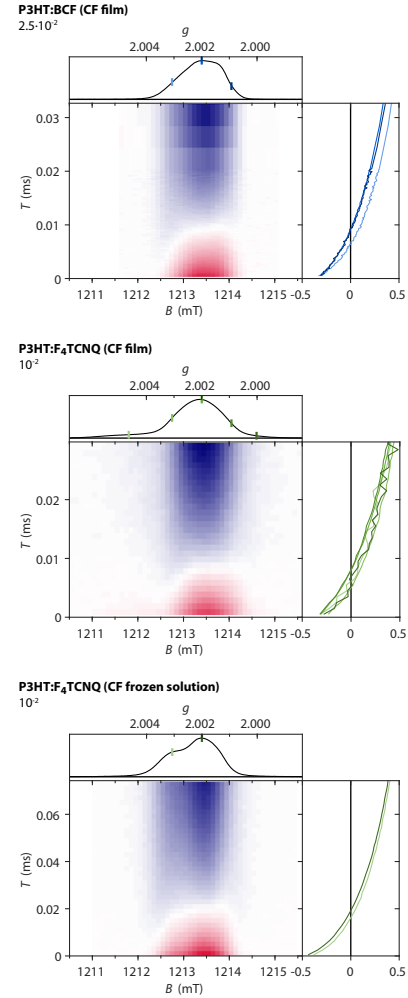


Fig. S7 Inversion recovery measurements as a function of magnetic field for a BCF-doped P3HT film and a F₄TCNQ-doped P3HT film and solution (CF) recorded at Q-band ($T = 10$ K). The initial part of the inversion recovery trace is shown and slices at different field positions are compared in the side panels (after normalisation to the mean intensity after full recovery).

S2.4 Pulse EPR spectra for doped P3HT in solution

The results of Q-band echo-detected pulse EPR measurements for frozen solutions of BCF- and F_4TCNQ -doped P3HT in oDCB and CF are compared in Fig. S8. The results are also compared to the spectrum recorded for the isolated F_4TCNQ radical anion in frozen THF solution. The spectra observed for F_4TCNQ -doped P3HT can be reconstructed as a linear combination of the spectrum for the corresponding BCF-doped sample and the spectrum of $F_4TCNQ^{\bullet-}$. In contrast to the significant differences in intensity between the spectra for F_4TCNQ -doped P3HT films prepared from oDCB or CF reported in the main text, the intensities of the spectra recorded for the two frozen solutions were comparable. The relative intensity of the $F_4TCNQ^{\bullet-}$ contribution compared to the $P3HT^{\bullet+}$ spectrum increases for increasing doping concentrations, as the relaxation time for $P3HT^{\bullet+}$, and correspondingly the overall echo intensity, decreases. In the case of F_4TCNQ -doped P3HT in oDCB solution at the highest doping ratio, only the $F_4TCNQ^{\bullet-}$ signal is observed, while for the corresponding CF solution both contributions are still visible. Doping-induced aggregation in highly doped P3HT solutions is well-known to occur and was clearly visible in the samples used for the EPR measurements, therefore the EPR results on frozen solutions are expected to converge towards the results obtained for the corresponding films. The absence of a $P3HT^{\bullet+}$ signal for the oDCB solution with the highest doping concentration and the significantly lower echo intensities in the films prepared from this solvent are therefore consistent and suggest differences in the morphology of the aggregates and then films prepared from this solvent, compared to those prepared from CF, that lead to increased relaxation and prevent echo-detected pulse EPR measurements.

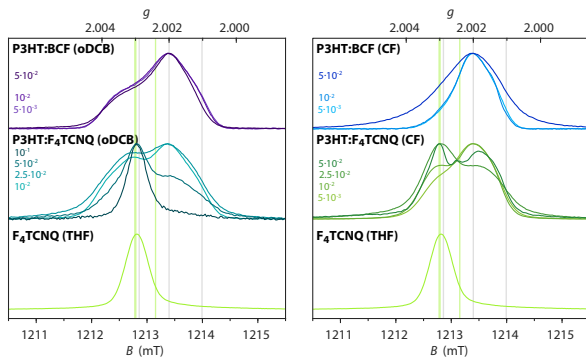


Fig. S8 Q-band echo-detected field-swept EPR spectra recorded for frozen solutions of P3HT doped with BCF and F_4TCNQ in oDCB and CF at different doping ratios ($T = 10$ K). The Q-band echo-detected spectrum recorded for the F_4TCNQ radical anion in THF solution is shown at the bottom for comparison. The grey and green vertical lines indicate the principal g -values determined for the P3HT radical cation and F_4TCNQ radical anion, respectively.

S2.5 Echo- and FID-detected pulse EPR spectra

Echo and FID transients recorded as a function of magnetic field for BCF- and F_4 TCNQ-doped P3HT films are compared in Fig. S9 along with the corresponding spectra obtained by Fourier transform and projection onto the field axis as described by Bowman et al.⁶ The relative intensity of the echo signal compared to the FID decreases significantly for increasing doping ratios for all dopant-solvent combinations, and for the F_4 TCNQ-doped P3HT films no echo signal could be detected at doping ratios above $2.5 \cdot 10^{-2}$. In all cases, the spectra determined from the echo and FID transients for the lowest shown doping ratio of 10^{-2} , as well as the spectra obtained by echo integration, are essentially identical.

For both BCF- and F_4 TCNQ-doped P3HT films, at higher doping ratios the FID transients contain an additional contribution with alternating positive and negative signal intensities. The FID transients shown in Fig. S9 were recorded after a soft, selective 200 ns pulse; Fig. S10 contains a comparison with the FID transients obtained for a harder 32 ns pulse for selected samples. For the shorter excitation pulse of 32 ns, the FID corresponding to the inhomogeneously broadened $P3HT^{\bullet+}$ signal observed via echo detection decays within the deadtime and is thus not observed, while for the 200 ns pulse it extends beyond the deadtime. The FID contribution observed for both types of pulses is due to a different species characterised by a narrower, possibly homogeneously broadened, EPR line.

The EPR spectrum derived from this FID signal for the BCF-doped P3HT film is characterised by partially resolved peaks at field positions corresponding to the principal values of the P3HT g -matrix, with increased intensity for the peak corresponding to the lowest g -value (g_x) as also observed in the W-band cw EPR data recorded on film samples and attributed to partial alignment.

For the F_4 TCNQ-doped P3HT films, the additional FID signal and the corresponding spectrum are centred at $g = 2.0027$, the same g -value as the single EPR line observed in X- and W-band cw EPR spectra for films obtained with this dopant.

Fig. S11 compares FID-detected inversion recovery measurements on this signal with echo-detected inversion recovery measurements on the $P3HT^{\bullet+}$ signal and shows spin-lattice relaxation times reduced by factors of about 40 and 10 for F_4 TCNQ-doped P3HT films prepared from oDCB at doping ratios of $2.5 \cdot 10^{-2}$ and $5 \cdot 10^{-2}$, respectively. Assuming the FID to be due to a homogeneous line, a spin-spin relaxation time T_m of about 10 to 20 ns can be estimated from the signal decay. The spin centres contributing to the FID signal therefore appear to be characterised by increased relaxation compared to the hole on P3HT observed via echo detection. This would be in agreement with assignment of this signal to exchange-coupled P3HT and F_4 TCNQ, which constitute the main contribution of the cw EPR signals for F_4 TCNQ-doped P3HT films.

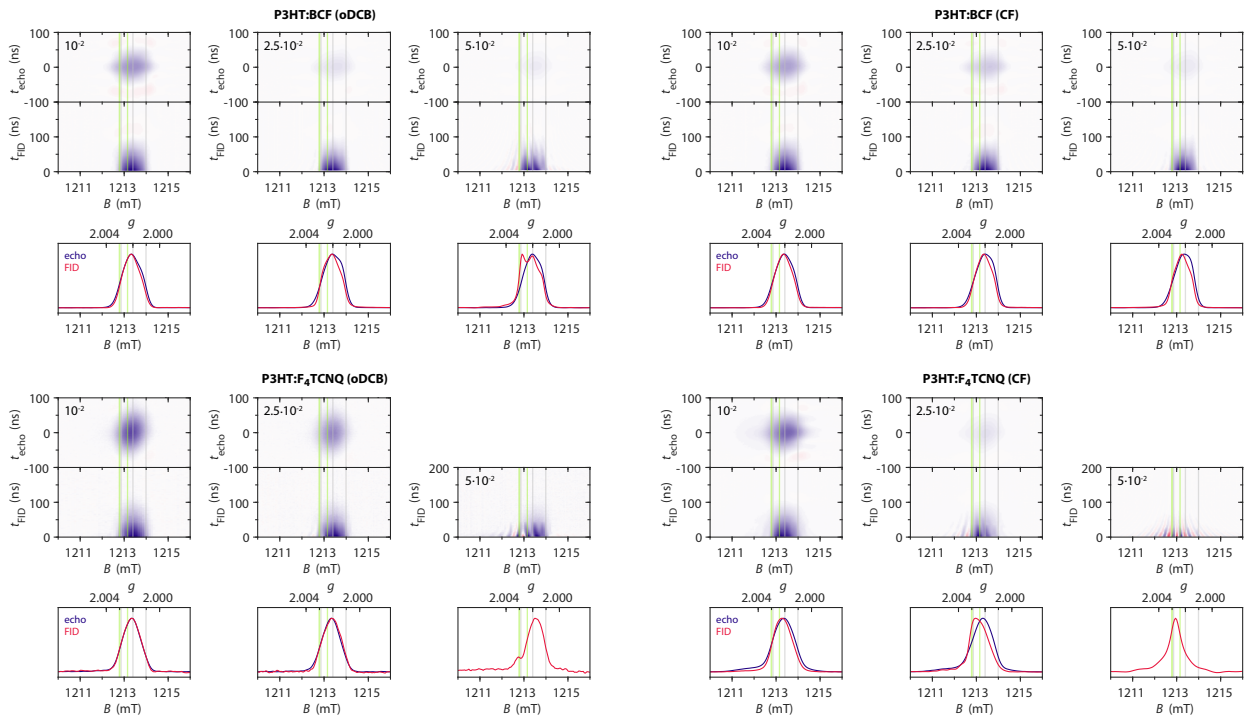


Fig. S9 Echo and FID transients recorded as a function of field at Q-band ($T = 10$ K) for BCF- and F_4 TCNQ-doped P3HT films prepared from oDCB or CF at different doping ratios and comparison of the echo and FID skew projection spectra obtained by Fourier transform of the corresponding transients and projection onto the magnetic field axis according to the procedure described by Bowman et al.⁶ The echoes were recorded for a pulse sequence with $t_\pi = 2t_{\pi/2} = 64$ ns and $\tau = 400$ ns, the FIDs were recorded after a $t_{\pi/2} = 200$ ns pulse. The intensities are scaled to match the experimentally observed relative intensities of the FID and echo signals for each doping ratio. The grey and green vertical lines indicate the principal g -values determined for $P3HT^{\bullet+}$ and $F_4TCNQ^{\bullet-}$, respectively.

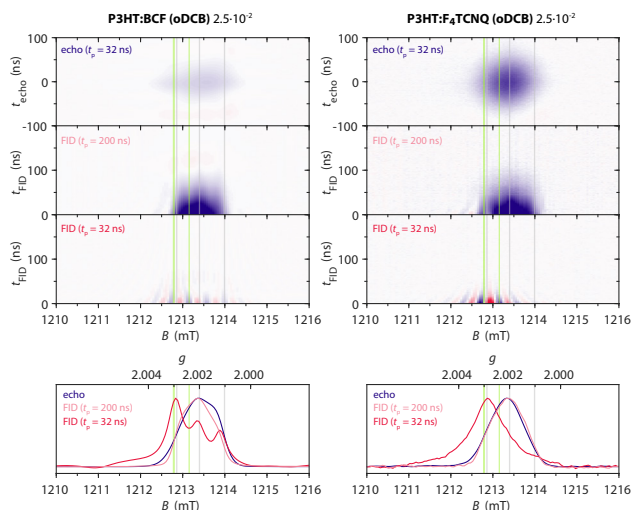


Fig. S10 Echo ($t_{\pi} = 2t_{\pi/2} = 64$ ns, $\tau = 400$ ns) and FID ($t_{\pi/2} = 32$ ns and $t_{\pi/2} = 200$ ns) transients recorded as a function of field at Q-band ($T = 10$ K) for BCF- and F_4 TCNQ-doped P3HT films at a doping ratio of $2.5 \cdot 10^{-2}$ (prepared from oDCB) and comparison of the corresponding skew projection spectra. The intensities are scaled to match the experimentally observed relative intensities of the FID and echo signals for each sample. The grey and green vertical lines indicate the principal g -values determined for $P3HT^{\bullet+}$ and $F_4TCNQ^{\bullet-}$, respectively.

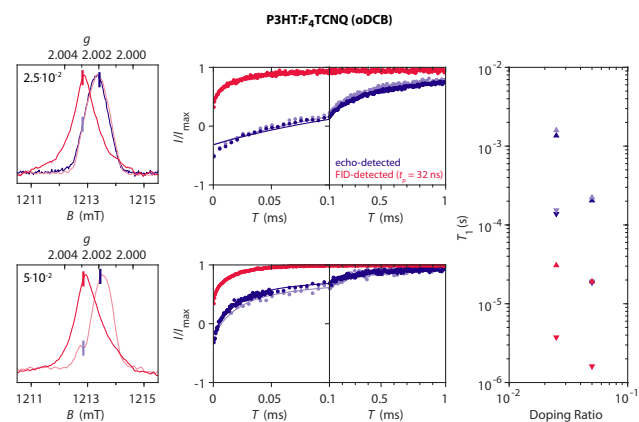


Fig. S11 Echo- and FID-detected Q-band inversion recovery data for F_4 TCNQ-doped P3HT films prepared from oDCB at doping ratios of $2.5 \cdot 10^{-2}$ and $5 \cdot 10^{-2}$ ($T = 10$ K). The inversion recovery measurements were performed with an inversion pulse $t_{\pi} = 64$ ns and detection sequences with $t_{\pi} = 2t_{\pi/2} = 128$ ns and $t_{\pi/2} = 32$ ns for echo and FID detection, respectively. The field positions for the measurements are indicated with respect to the echo and FID skew projection spectra shown in the panels on the left. The T_1 values determined from a biexponential fit of the inversion recovery traces are plotted on the right.

S2.6 Q-band ^1H ENDOR measurements

Fig. S12 and Fig. S13 show the dependence of the ^1H Davies ENDOR spectrum for BCF-doped P3HT films prepared from oDCB at a doping ratio of 10^{-2} on temperature and on magnetic field position. No changes in the ENDOR spectrum could be detected within the range of temperatures for which the experiment could be performed. A comparison of ENDOR spectra recorded at different magnetic fields across the P3HT $^{\bullet+}$ spectrum at Q-band only shows minor orientation selection effects, as also previously observed at W-band.¹¹

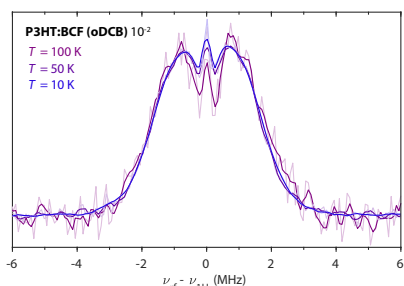


Fig. S12 Q-band ^1H Davies ENDOR spectra for a BCF-doped P3HT film prepared from oDCB at a doping ratio of 10^{-2} recorded at different temperatures ($T = 10\text{ K}$, 50 K and 100 K). The ENDOR spectra were recorded at the magnetic field position corresponding to the maximum of the P3HT radical cation signal.

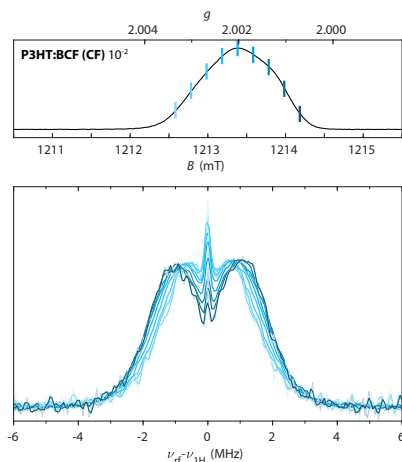


Fig. S13 Q-band ^1H Davies ENDOR spectra for a BCF-doped P3HT film prepared from oDCB at a doping ratio of 10^{-2} recorded at different field positions as indicated on the spectrum in the top panel ($T = 10\text{ K}$).

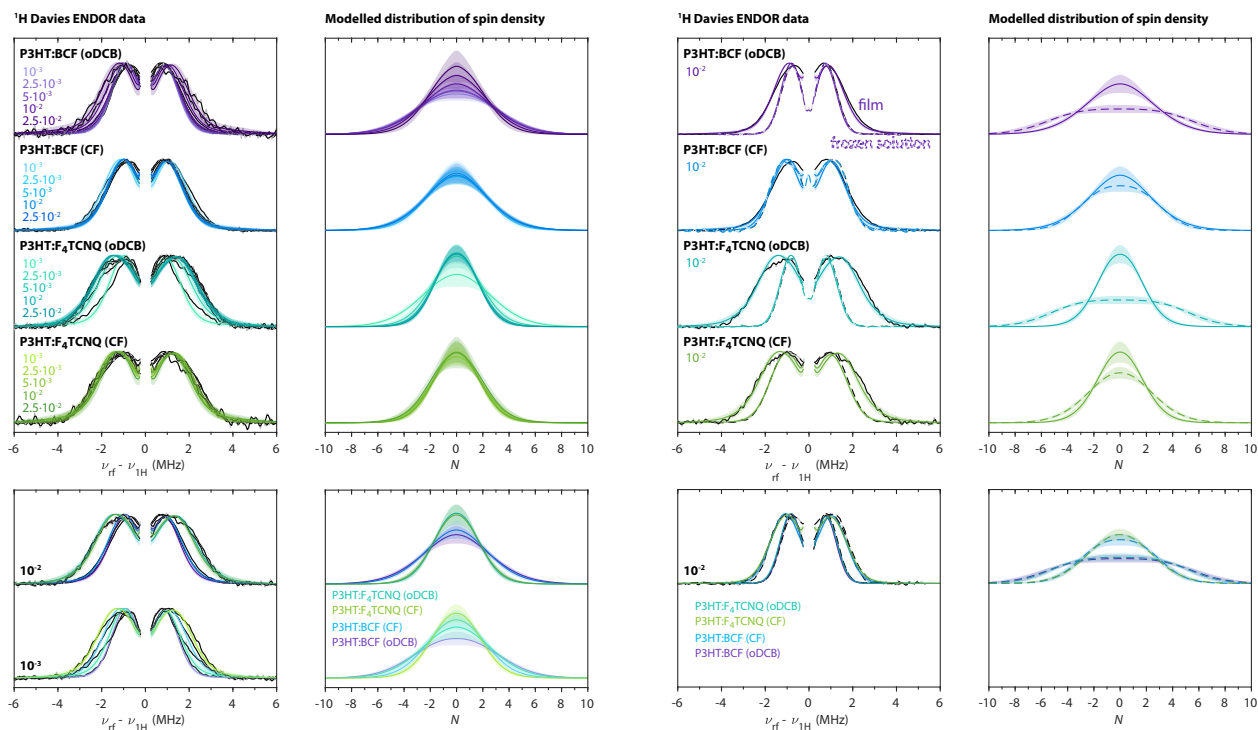


Fig. S14 Results of the determination of the extent of spin delocalisation from the Q-band ^1H ENDOR data for BCF- and F_4TCNQ -doped P3HT films (solid lines) and solutions (dashed lines). The experimental spectra are compared to the best-fit ENDOR simulations calculated for the range of distributions of spin densities along N thiophene units of the P3HT backbone shown in the panels on the right of the experimental data. The results are compared for each dopant-solvent pair at different doping ratios (*top-left*), for films samples and the corresponding frozen solutions (*top-right*), for films with different dopant-solvent combinations at selected doping ratios (*bottom-left*) and for solutions with different dopant-solvent combinations at a selected doping ratio (*bottom-right*). The shaded regions depict the range of distributions and simulated ENDOR spectra in agreement with the experimental data.

S2.7 EPR characterisation of the F₄TCNQ radical

The F₄TCNQ radical anion generated by ionisation in THF solution was characterised by cw and pulse EPR to aid identification of contributions from F₄TCNQ^{•-} in the EPR data obtained for F₄TCNQ-doped P3HT. The results of multifrequency cw EPR measurements on solutions and films, as well as Davies ENDOR and three-pulse ESEEM measurements are shown in Fig. S15.

The solution cw EPR spectra recorded at X- and W-band show a clearly resolved hyperfine structure arising from the hyperfine coupling to the four equivalent fluorine and the four equivalent nitrogen nuclei in the F₄TCNQ molecule. The isotropic *g*-value and the isotropic hyperfine coupling constants *a*_{iso} for the two types of nuclei could be accurately determined from comparison with simulations and are reported in Table S1.

The W-band cw EPR spectra recorded on a frozen solution of F₄TCNQ in THF and on a film obtained after evaporation of the solvent under vacuum are characterised by an approximately axial *g*-matrix. The orientation of the *g*-matrix in the molecular frame is determined by the symmetry of the molecule, as confirmed by DFT calculations at the B3LYP/EPR-III level of theory^{20,21}, and is depicted in Fig. S15.

The principal values of the ¹⁹F hyperfine coupling matrix were determined from a global fit of Q-band Davies ENDOR and field-dependent W-band Davies ENDOR measurements. The principal values of the ¹⁴N hyperfine coupling matrix were estimated based on a global fit of the time- and frequency-domain Q-band three-pulse ESEEM data from measurements performed for different τ

values on the signal maximum. The nuclear quadrupole interaction parameters for ¹⁴N, as well as the orientations of the hyperfine coupling and nuclear quadrupole matrices were fixed at the values determined by DFT calculations.

Table S1 Experimentally determined *g*-values, hyperfine and nuclear quadrupole coupling parameters for the ¹⁹F and ¹⁴N nuclei in the F₄TCNQ radical anion.

		¹⁴ N	¹⁹ F
<i>g</i> _{iso}	2.00280	<i>a</i> _{iso} (MHz)	3.13 ± 0.05
<i>g</i> _{<i>x</i>}	2.0030	<i>A</i> _{<i>x</i>} (MHz)	-1.17 ± 0.10
<i>g</i> _{<i>y</i>}	2.0030	<i>A</i> _{<i>y</i>} (MHz)	-1.87 ± 0.10
<i>g</i> _{<i>z</i>}	2.0024	<i>A</i> _{<i>z</i>} (MHz)	12.43 ± 0.10
		<i>e</i> ² <i>Qq</i> / <i>h</i> (MHz)	-1.00 ± 0.10
		η	0.33 ± 0.10

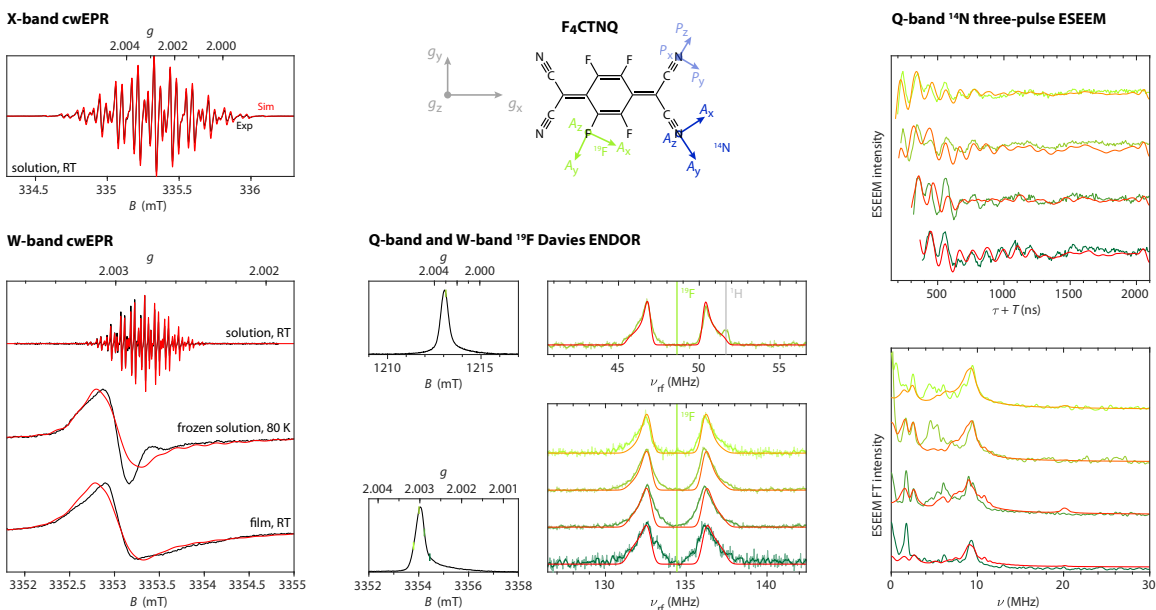


Fig. S15 Characterisation of the F₄TCNQ radical anion by EPR, ENDOR and ESEEM at multiple frequencies. (*top, centre*) Molecular structure of F₄TCNQ and principal axes of the *g*-matrix, ¹⁹F hyperfine matrix and ¹⁴N hyperfine and nuclear quadrupole matrices. (*left*) Experimental X- and W-band cw EPR spectra recorded on solutions of F₄TCNQ in THF-*d*₈ (0.25 mg mL⁻¹) at room temperature and 80 K and on a film. (*centre*) Q- and W-band Davies ENDOR spectra recorded on frozen solutions of F₄TCNQ in THF-*d*₈ at 40 K and 80 K, respectively. The field positions for the ENDOR measurements are indicated with respect to the echo-detected field-swept spectra. (*right*) Q-band three-pulse ESEEM time traces and spectra recorded on a frozen solution of F₄TCNQ in THF-*d*₈ at 40 K for τ values of 118 ns, 142 ns, 238 ns and 302 ns. The experimental results are compared to simulations (in red-orange) with parameters optimised by a global fit and listed in Table S1.

S2.8 Additional ENDOR and ESEEM data for F₄TCNQ-doped P3HT

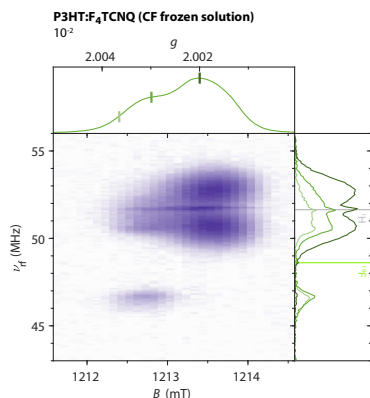


Fig. S16 Q-band Davies ENDOR recorded as a function of magnetic field for P3HT doped with F₄TCNQ in chloroform solution at a doping ratio of 10^{-2} ($T = 10$ K). Slices selected at the indicated field positions are compared in the side panel and show contributions from ¹H and ¹⁹F nuclei coupled to the P3HT radical cation and the F₄TCNQ radical anion, respectively.

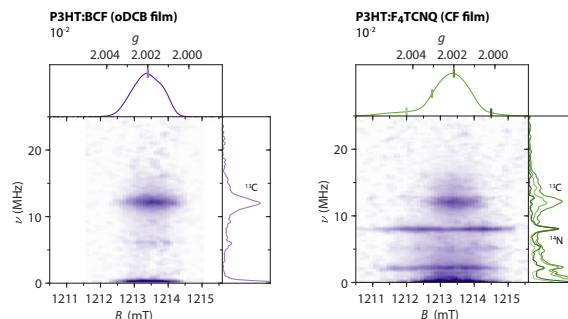


Fig. S18 Three-pulse ESEEM spectra recorded as a function of magnetic field for a BCF-doped P3HT film (from oDCB) and a F₄TCNQ-doped P3HT film (from CF) at Q-band ($T = 10$ K). ESEEM traces were recorded for τ values of 140 ns, 180 ns and 240 ns and summed after FT. The signals around 13 MHz observed for both samples at field positions corresponding to the P3HT radical cation are assigned to contributions from natural abundance ¹³C.

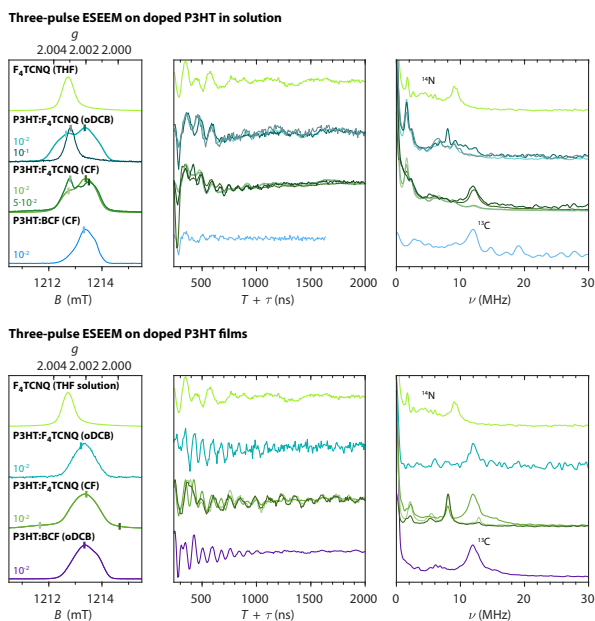


Fig. S17 Three-pulse ESEEM time domain traces and FT spectra recorded at Q-band for BCF- and F₄TCNQ-doped P3HT solutions and films ($T = 10$ K). ESEEM traces were recorded at different field positions indicated by the markers on the EPR spectra. The three-pulse ESEEM data recorded on the F₄TCNQ radical anion in THF solution is shown for comparison. The time traces are shown for $\tau = 140$ ns and the frequency domain spectra are the summed over τ values of 140 ns, 180 ns and 240 ns.

S2.9 Additional PEANUT measurements and simulations

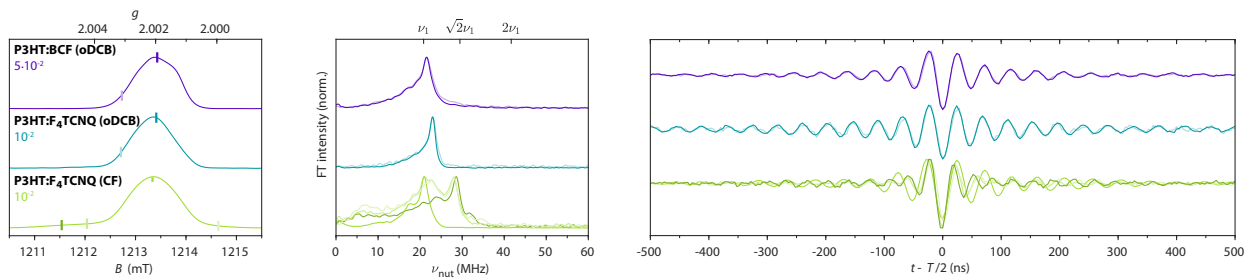
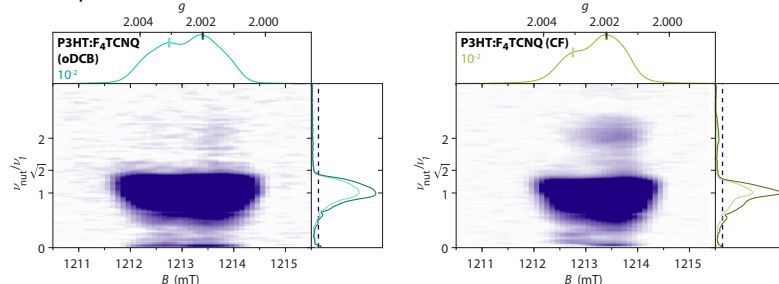


Fig. S19 EPR spectra (*left*) and frequency- (*centre*) and time-domain (*right*) data recorded at Q-band ($T = 10$ K) for BCF- and F₄TCNQ-doped P3HT films prepared from oDCB or CF. The results of PEANUT measurements at different field positions indicated on the corresponding spectra are compared for each sample.

PEANUT on doped P3HT solutions



PEANUT on doped P3HT films

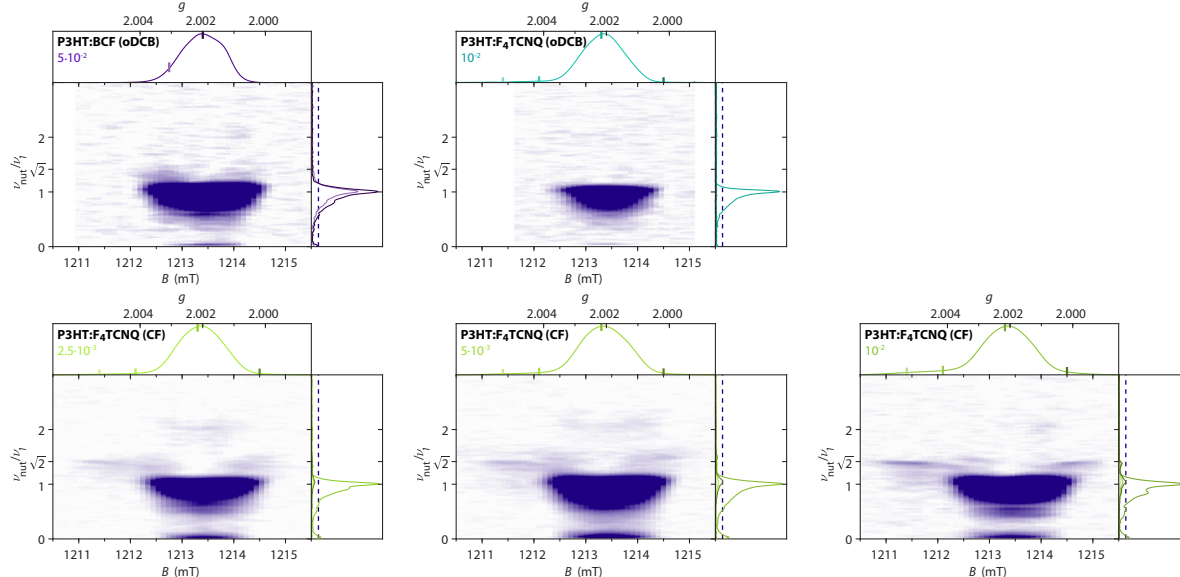


Fig. S20 Q-band two-dimensional PEANUT data for P3HT films and solutions doped with BCF and F₄TCNQ prepared from oDCB or CF ($T = 10$ K). For a better display of the weak contributions from the broad underlying signal in the film prepared from CF, the intensities in the 2D plots are clipped at 10% of the maximum intensity (marked by a dashed line in the side panels). The experimental nutation frequency for an $S = \frac{1}{2}$ spin centre corresponds to $\nu_1 \approx 21$ MHz.

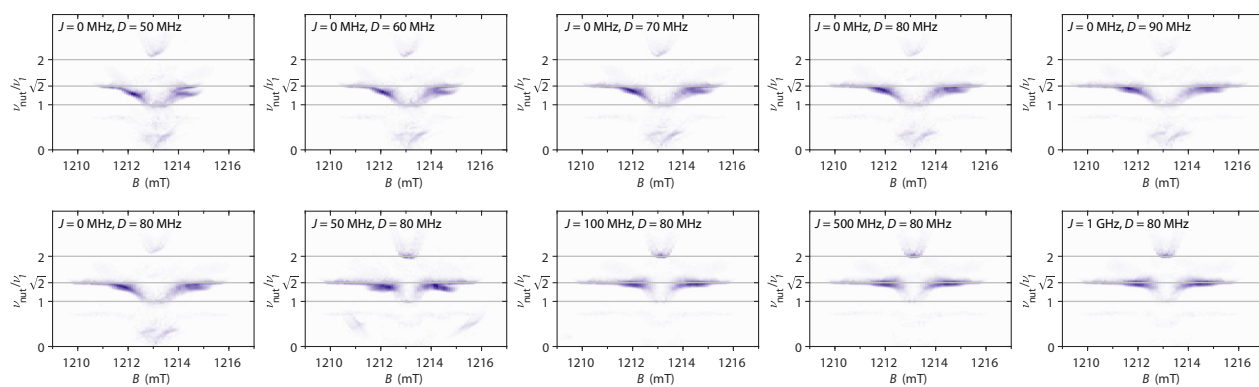


Fig. S21 Simulations of two-dimensional Q-band PEANUT spectra for a pair of coupled P3HT and F₄TCNQ radicals with different dipolar and exchange coupling strengths. The principal g -values used for the simulations were $g_x = 2.0029$, $g_y = 2.0020$ and $g_z = 2.0010$ for P3HT and $g_x = 2.0030$, $g_y = 2.0030$ and $g_z = 2.0024$ for F₄TCNQ, the relative orientation of the molecules used for the simulations corresponds to an orthogonal arrangement of P3HT and F₄TCNQ as described by Hamidi-Sakr et al.¹⁸

References

- 1 M. Arvind, C. E. Tait, M. Guerrini, J. Krumland, A. M. Valencia, C. Cocchi, A. E. Mansour, N. Koch, S. Barlow, S. R. Marder, J. Behrends and D. Neher, *J. Phys. Chem. B*, 2020, **124**, 7694–7708.
- 2 J. J. Wittmann, T. V. Can, M. Eckardt, W. Harneit, R. G. Griffin and B. Corzilius, *J. Magn. Reson.*, 2018, **290**, 12–17.
- 3 G. R. Eaton, S. S. Eaton, D. P. Barr and R. T. Weber, *Quantitative EPR*, Springer-Verlag, Wien, 2010.
- 4 T. J. Prosa, M. J. Winokur, J. Moulton, P. Smith and A. J. Heeger, *Macromolecules*, 1992, **25**, 4364–4372.
- 5 E. J. Reijerse, F. Lendzian, R. A. Isaacson and W. Lubitz, *J. Magn. Reson.*, 2012, **214**, 237–243.
- 6 M. K. Bowman, M. D. Krzyaniak, A. A. Cruce and R. T. Weber, *J. Magn. Reson.*, 2013, **231**, 117–125.
- 7 S. Van Doorslaer, G. A. Sierra and A. Schweiger, *J. Magn. Reson.*, 1999, **136**, 152–158.
- 8 S. Stoll and A. Schweiger, *J. Magn. Reson.*, 2006, **178**, 42–55.
- 9 S. Stoll, G. Jeschke, M. Willer and A. Schweiger, *J. Magn. Reson.*, 1998, **130**, 86–96.
- 10 S. Stoll and R. D. Britt, *Phys. Chem. Chem. Phys.*, 2009, **11**, 6614–6625.
- 11 A. Aguirre, P. Gast, S. Orlinskii, I. Akimoto, E. J. J. Groenen, H. El Mkami, E. Goovaerts and S. Van Doorslaer, *Phys. Chem. Chem. Phys.*, 2008, **10**, 7129–7138.
- 12 H. M. McConnell and D. B. Chesnut, *J. Chem. Phys.*, 1958, **28**, 107–117.
- 13 J. R. Morton, *Chem. Rev.*, 1964, **64**, 453–471.
- 14 V. M. Geskin, A. Dkhissi and J.-L. Brédas, *Int. J. Quantum Chem.*, 2003, **91**, 350–354.
- 15 J. Niklas, K. L. Mardis, B. P. Banks, G. M. Grooms, A. Sperlich, V. Dyakonov, S. Beaupré, M. Leclerc, T. Xu, L. Yu and O. G. Poluektov, *Phys. Chem. Chem. Phys.*, 2013, **15**, 9562–9574.
- 16 C. Fan, P. E. Doan, C. E. Davoust and B. M. Hoffman, *J. Magn. Reson.*, 1992, **98**, 62–72.
- 17 S. Pribitzer, A. Doll and G. Jeschke, *J. Magn. Reson.*, 2016, **263**, 45–54.
- 18 A. Hamidi-Sakr, L. Biniek, J. L. Bantignies, D. Maurin, L. Herrmann, N. Leclerc, P. Lévêque, V. Vijayakumar, N. Zimmermann and M. Brinkmann, *Adv. Funct. Mater.*, 2017, **27**, 1700173–1–13.
- 19 P. S. Marqués, G. Londi, B. Yurash, T.-Q. Nguyen, S. Barlow, S. R. Marder and D. Beljonne, *Chem. Sci.*, 2021, **12**, 7012–7022.
- 20 F. Neese, *ORCA – an ab initio, Density Functional and Semiempirical program package*, 2011.
- 21 F. Neese, *WIREs: Comput. Mol. Sci.*, 2018, **8**, e1327–1–6.